symmetry

MDPI

Article

Particle Multiplicity Fluctuations and Spatiotemporal Properties of Particle-Emitting Source of Strongly Interacting Matter for NICA and RHIC Energies

Mariya Cheremnova [1], Alexey Chernyshov [1], Yevheniia Khyzhniak [2], Olga Kodolova [1,*], Valentin Kuzmin [1], Igor Lokhtin [1], Ludmila Malinina [1,3], Konstantin Mikhaylov [3,4] and Grigory Nigmatkulov [2,3]

[1] Department of Expiremental High Energy Physics, Skobeltsyn Institute of Nuclear Physics, Federal State Budget Educational Institution of Higher Education M.V. Lomonosov Moscow State University, SINP MSU 1(2), Leninskie Gory, GSP-1, 119991 Moscow, Russia; mariya.cheremnova@mail.ru (M.C.); ach1999@yandex.ru (A.C.); valentin-a-kuzmin@yandex.com (V.K.); igor.lokhtin@cern.ch (I.L.); ludmila.malinine@cern.ch (L.M.)

[2] Department of Experimental Nuclear Physics and Cosmophysics, National Research Nuclear University MEPhI, 31 Kashirskoe Shosse, 115409 Moscow, Russia; eugenia.sh.el@gmail.com (Y.K.); nigmatkulov@gmail.com (G.N.)

[3] Veksler and Baldin Laboratory of High Energy Physics, Joint Institute for Nuclear Research, Joliot-Curie st., 6, 141980 Dubna, Russia; konstantin.mikhaylov@cern.ch

[4] Laboratory of Relativistic Nuclear Physics, National Research Center "Kurchatov Institute", pl. Kurchatova, 1, 123182 Moscow, Russia

* Correspondence: olga.kodolova@cern.ch

check for updates

Citation: Cheremnova, M.; Chernyshov, A.; Khyzhniak, Y.; Kodolova, O.; Kuzmin, V.; Lokhtin, I.; Malinina, L.; Mikhaylov, K.; Nigmatkulov, G. Particle Multiplicity Fluctuations and Spatiotemporal Properties of Particle-Emitting Source of Strongly Interacting Matter for NICA and RHIC Energies. *Symmetry* **2022**, *14*, 1316. https://doi.org/10.3390/sym14071316

Academic Editor: Kazuharu Bamba

Received: 11 May 2022
Accepted: 16 June 2022
Published: 25 June 2022

Abstract: The results of the model analysis of hadron femtoscopic correlations and factorial moments of particle multiplicity in heavy ion collisions for the energy range of the Beam Energy Scan (BES) program at RHIC and future NICA collider are presented. For this purpose, the simulation of Au+Au collisions at center-of-mass energies 7.7 and 11.5 GeV per nucleon pair using the UrQMD, vHLLE+UrQMD (with the crossover and first-order equation of states), and HYDJET++ event generators was performed. The sensitivity of pion and kaon correlation radii and the dependence of the factorial moments on heavy ion beam energy to quark–hadron phase transition details was studied. In addition, the possible influence of some relevant detector effects on the corresponding experimental observables is discussed.

Keywords: correlation femtoscopy; intermittency; fluctuations; strongly interacting matter

1. Introduction

Experiments at the Relativistic Heavy Ion Collider (RHIC) [1–4] and later at the Large Hadron Collider (LHC) [5–7] demonstrated that nuclear collisions create a medium known as Quark–Gluon Plasma (QGP), which consists of deconfined strongly interacting quarks and gluons. The properties of the QGP must be quantified in order to describe the Quantum Chromodynamics (QCD) phase diagram [8], which can be expressed in terms of temperature (T) and baryon chemical potential (μ_B). At low baryon densities, $\mu_B \approx 0$ MeV, which correspond to the top RHIC and LHC energies, lattice QCD calculations [9] predict a smooth Crossover Transition (XPT) from nuclear matter to QGP. At finite μ_B, corresponding to the lower collision energies, the phase transition is expected to be of the first order (1PT) [10], which would also imply the existence of the critical end point [11].

From the experimental point of view, different regions of the QCD phase diagram can be accessed by colliding heavy ions at different energies. To achieve this goal, beam energy scan programs have been initiated at the existing accelerators (SPS and RHIC), as well as at the future NICA and FAIR facilities. Depending on the collision energy, the matter spends different times in a QGP, mixed, or hadronic phase. The duration for which the system stays at each phase may imprint a signal on various observables that could be searched for the non-monotonic behavior as a function of beam energy.

Theoretically, it is predicted that the event-by-event fluctuations of conserved quantities such as net baryon, net strangeness, and net charge should depend on the non-equilibrium correlation length, ξ, and will play the role of sensitive observables of critical behavior [12]. Transition from QGP to hadronic matter was predicted from the first principles lattice QCD calculations to be a smooth crossover at $\sqrt{s_{NN}} \geq 39$ GeV [13,14]. Recently, it was experimentally confirmed noticing that the sign net-proton higher-order cumulant ratio C_6/C_2 was negative [15]. At the vicinity of the critical point, the correlation length should grow as large as the system size. On the other hand, the effects of the finite size and finite time of the medium will limit the significance of the signals [16]. However, it was experimentally demonstrated that the higher-order net-proton cumulant ratio C_4/C_2 exhibits a non-monotonic behavior as a function of beam energy [17].

Another method to suppress statistical fluctuations was proposed by A. Bialas and R. Peschanski [18]. The dependence of the normalized factorial moments of the multiplicity distribution (M) in bins over phase space on the bin size (intermittency) appears, revealing dynamical fluctuations in the underlying process. Factorial moments were studied in [19,20], and the rise of the factorial moments as a function of multiplicity was observed. Recently, intermittency was studied for heavy ion collisions by the SHINE/NA61 Collaboration [21]. It was proposed to use this method to distinguish between different types of phase transitions [22,23]. Other observables that are sensitive to the type of phase transition are the sizes and shapes of the particle-emitting source created at freeze-out [24]. At the femtometer scale, correlation femtoscopy technique allow obtaining access to the final-state geometry (femtoscopic radii) of a nuclear collision [25–27]. Due to pressure-driven bulk collective flow, detailed measurements of this geometry as a function of transverse momentum (p_T), rapidity (y), and particle mass have revealed a rich spatial substructure of the system. The method has grown into a precise tool [28] for assessing the spatial and temporal properties of homogeneity regions [29,30] during kinetic freeze-out in heavy ion collisions by extracting femtoscopic radii using two-particle momentum correlations. Femtoscopic measurements of identical pions at top RHIC [31] and LHC [32] demonstrated that emitting-source radii decrease with increasing pair transverse momentum due to the collective flow in heavy ion collisions. The identical kaon analyses are expected to provide a cleaner probe as compared to pions because they are less affected by resonance decays. Theoretical calculations [33] and experimental experimental measurements [34] at LHC energies demonstrated that kaon radii can be described only if the hadronic rescattering phase follows the hydrodynamic phase [35].

It was theoretically demonstrated that the femtoscopic radii are sensitive to the long duration of particle emission due to a first-order phase transition that could be imprinted in the energy dependence [36–38]. This was not supported by RHIC data [39,40] and then led to the essential revision of the hydrodynamic models [41]. Since then, several aspects were found to be important: the presence of prethermal transverse flow, a crossover phase transition between quark–gluon and hadron matters for high RHIC and LHC energies [42], the non-hydrodynamic behavior of the hadron gas at the latest stage, and correct matching between hydrodynamic and non-hydrodynamic stages [43–45]. The recent theoretical considerations [46] demonstrate that the first-order quark–hadron phase transition can lead to a reasonable description of some bulk observables, but there is a lack of such a study for femtoscopy (especially for heavier-than-pion particles).

The excitation function of pion femtoscopic radii (R_{out} and R_{side} in outward and sideward directions, respectively) measured by STAR [47] demonstrates a non-monotonic behavior of R_{out}/R_{side} as a function of Au+Au collision energy ($\sqrt{s_{NN}}$), while it can be well described within the hybrid approach using the vHLLE+UrQMD model [48].

In this paper, we present the model calculations of pion and kaon femtoscopic radii for Au+Au collisions at $\sqrt{s_{NN}} = 7.7$ and 11.5 GeV that are in the energy range of the second phase of beam energy scan (BES) program at RHIC and the NICA facility. In addition, we explore the multiparticle correlation based on the normalized factorial moments of the charged particles' rapidity distribution. We present normalized factorial moments' dependence on the number of particles for the first-order phase transition and crossover for the NICA facility with model calculations for Au+Au collisions.

2. Materials and Methods

2.1. Simulation of Heavy Ion Collisions

In order to investigate the sensitivity of the femtoscopic radii and factorial moments to the nature of the phase transition, the three Monte Carlo event generators UrQMD [49,50] and vHLLE+UrQMD [51] were utilized. In order to test the sensitivity of factorial moments to particle multiplicity and freeze-out conditions, the HYDJET++ event generator [52] was used.

The UrQMD model is a microscopic transport theory that combines the covariant propagation of hadrons on classical trajectories with stochastic binary scatterings, the formation of color strings, and resonance decays.

The vHLLE+UrQMD is a hybrid model that uses UrQMD for the early and late non-equilibrium stages of the reaction and (3 + 1)-dimensional viscous hydrodynamics for the hot and dense quark–gluon matter stage. The model uses two types of the Equation of State (EoS): chiral model EoS [53] and bag model EoS [54]. The chiral model EoS includes a crossover-type transition between quark–gluon matter and hadronic phases for all baryon densities. The bag model EoS considers a first-order phase transition between the phases. In this work, we will refer to the former type of phase transition as "XPT EoS" and to the latter as "1PT EoS", respectively. The difference between the two EoS was discussed in, e.g., [46]. It was shown that for the 1PT EoS, the average duration of hydrodynamic evolution is longer than for the XPT EoS due to the effect of the mixed phase that exists for bag model EoS. However, this difference is smeared up due to the hadronic rescatterings occurring after the hydrodynamic evolution. The shapes of rapidity distributions are equally well described by the vHLLE+UrQMD model with both EoSs for a wide heavy ion beam energy range. The calculations with 1PT EoS lead also to some suppression of the average radial flow as compared to XPT EoS. It can appear for smaller mean p_T (especially for high-p_T particles), smaller elliptic flow, and larger femtoscopic scales.

HYDJET++ is a two-component model, the final state in which represents a superposition of the soft "thermal" state and the hard state resulting from multi-parton fragmentation. The soft component of HYDJET++ is dominating for considered heavy ion beam energies. The thermal hadronic state generated on the chemical and thermal freeze-out hypersurfaces is obtained from hydro-type parameterization with preset freeze-out conditions. It includes the longitudinal, radial, and anisotropic flow effects and the decays of hadronic resonances. In the context of current study, we considered HYDJET++ as an approach "without phase transition", because such a transition is not specified explicitly in the model. Note, however, that the model freeze-out parameters obtained from fits of RHIC data may effectively correspond to a fluid dynamical evolution with phase transition.

In the current study, samples of approximately 30 million collisions of gold nuclei at $\sqrt{s_{NN}}$ = 7.7 and 11.5 GeV were generated and analyzed.

2.2. Correlation Femtoscopy

A direct study of the spatial and temporal structure at the kinetic freeze-out can be acquired using the femtoscopy technique. The method investigates two-particle momentum correlations in order to obtain information about the source function, $S(p, r^*)$. The source function represents the probability of emitting a pair of particles with total momentum (p) and relative distance (r^*). Under certain assumptions, the correlation function of two particles can be represented as [55]:

$$C(\vec{p},\vec{q}) = \int \mathrm{d}\vec{r}^{*} S(\vec{p},\vec{r}^{*}) |\Psi(\vec{q},\vec{r}^{*})|^2, \tag{1}$$

where Ψ is a two-particle wave function and $\vec{q}$ and $\vec{r}^*$ are the relative momentum and the particle separation in the pair reference frame, respectively. The source function is represented by the space–time distribution in the corresponding model. In this article, we study the correlations of pairs of charged pions and kaons. Only the quantum statistical effects for Ψ are taken into account [25–27]. The final state interactions (Coulomb and strong) are not considered. The corresponding square of the wave function is calculated as $|S(\vec{p},\vec{r}^*)\Psi(\vec{q},\vec{r}^*)|^2 = 1 + \cos(\Delta p \Delta x)$, where p and x are the four-momentum and four-coordinate of particles at kinetic freeze-out.

Two-particle correlations are studied in the Longitudinally Co-Moving System (LCMS), where the longitudinal momentum of each pair is equal to zero ($p_{z,1} + p_{z,2} = 0$ GeV/c). In the current study, a pair relative momentum q is decomposed into three projections (q_{out}, q_{side}, q_{long}) using Bertsch–Pratt (out-side-long) system [36,37]. The outward direction is pointing along the pair transverse momentum ($k_T = p_{1,T} + p_{2,T}$); the longitudinal direction is pointing along the beam direction; sideward axis is orthogonal to the other two.

In order to extract femtoscopic radii, the obtained correlation functions are fit to:

$$C(q_{out}, q_{side}, q_{long}) = \kappa\Big(1 + \lambda \exp(-R_{out}^2 q_{out}^2 - R_{side}^2 q_{side}^2 - R_{long}^2 q_{long}^2)\Big), \tag{2}$$

where κ is a normalization factor, λ represents the correlation strength, and R_{out}, R_{side}, and R_{long} are the femtoscopic radii in outward, sideward, and longitudinal directions, respectively. R_{out} is sensitive to the geometrical size and duration of particle emission; R_{side} is proportional to the geometrical size of particle-emitting region; R_{long} is related to the time of the maximum emission.

Figure 1 demonstrates an example of the two-pion (red open stars) and two-kaon (blue solid stars) three-dimensional correlation function projections onto the out (left panel), side (middle panel), and long (right panel) directions. The correlation function have been obtained for the 0–10% central Au+Au collisions simulated in the UrQMD model.

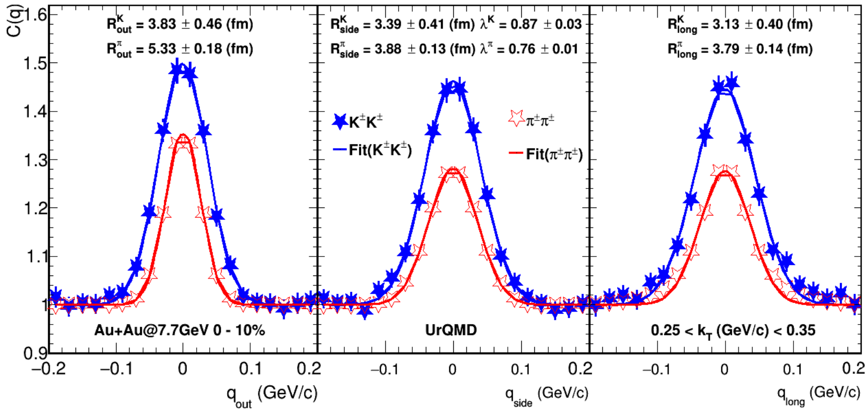

Figure 1. Out (**left panel**), side (**middle panel**), and long (**right panel**) projections of the three-dimensional correlation functions of identical pions (red open stars) and kaons (blue solid stars) estimated for 0–10% central Au+Au collisions at $\sqrt{s_{NN}}$ = 7.7 GeV using the UrQMD model. Solid lines represent fit projections.

Correlation functions of positively and negatively charged pairs of identical particles were constructed and found to be comparable within statistical uncertainties. Figure 1 uses the positively and negatively charged pairs combined in order to increase the precision of the measurements. Numerators of charged pairs were summed before constructing the ratio. The same procedure was applied for the denominators. Red and blue solid lines represent out, side, and long projections of the fit using Equation (2) to the correlation function. The correlation function shown in Figure 1 is obtained for pairs with transverse momentum $k_T = 0.5(p_{T,1} + p_{T,2})$ in the range from 0.25 to 0.35 GeV/c. The measurement of femtoscopic radii dependence on k_T or the transverse mass of the pair ($m_T = \sqrt{k_T^2 + m^2}$, where m is the mass of the particle of the given species) allows studying the dynamics of the emitting source evolution [29].

2.3. Experimental Effects Affecting Femtoscopic Observables

Similar to other physics observables, femtoscopic radii are affected by the experimental effects. In this work, we estimated the influence of detector effects such as momentum resolution and a merging pair of tracks on the extracted parameters.

The problem arises from determining the parameters of two charged particles with close momenta, which can be experimentally limited by the detector resolution. The experimental solution of track separation may be restricted by the resolution of the detector. Modern experiments that aim to study the properties of strongly interacting matter [56,57] use Time Projection Chambers (TPCs) as the main tracking detector. The sensitive elements of such a chamber are located at the ends of its cylinder and form a ring bounded by the minimum and maximum radii R_{min} and R_{max}. In turn, the ring is divided into sectors, inside which the sensitive elements are located in rows parallel to the bases of a trapezoid inscribed in a sector. The resolution of the TPC is determined by the distance d_p between the centers of these sensitive elements. In order not to generate events with two close tracks, which the detector will not be able to reconstruct separately, we find a condition of the registration of such pairs by the TPC.

If $\mathbf{p_1}$ and $\mathbf{p_2}$ are the momenta of particles and $p = p_1 \simeq p_2$, d_{tr} is the width of the band left by the track on the plane of the TPC sensitive elements, and d_p is the distance between these elements (Figure 2). If $q_\perp = |\mathbf{p_1}_\perp - \mathbf{p_2}_\perp|$ and D_s is the distance from of the production point to a row of sensitive elements, then the distance L between the projections of tracks along this row is equal to the value $q_\perp D_s/p$. A sufficient condition for the separation of two tracks in the TPC will be the presence of two non-fired sensors between projections of tracks in the middle row of sensitive elements of the sector. Mathematically, this condition is written as an inequality:

$$q_\perp D_s/p_\perp > 2d_p + d_{tr}. \tag{3}$$

The use of the longitudinal component in the criterion of type (3) is complicated by the fact that the left part will be the value of the following order of smallness of the q/p value.

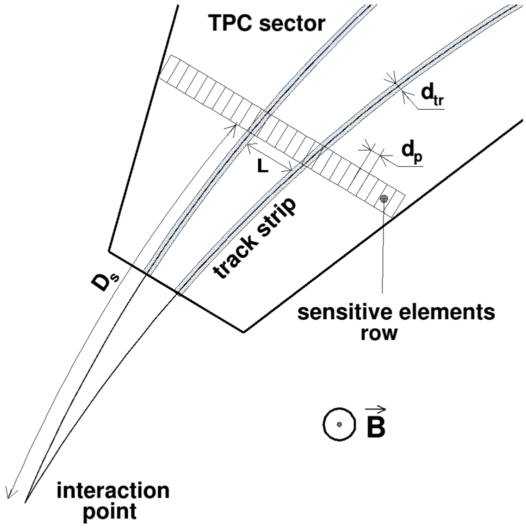

Figure 2. Schematic view of the trajectories of a track pair in a time projection chamber.

In our estimations, we assumed that the average size (d_p) of the TPC sensor (pad) is about 0.5 cm and the distance D_s from the chamber axis to the middle of the sector is about 90 cm [58–60]. Thus, d_{tr} should be about 0.6 cm, so the condition of the track separation in this detector is $q_\perp/p_\perp \approx 0.02$. Since the calculation is based on the ideal geometry and detector assumptions, it can be treated as an upper limit for the real situation.

Another important aspect is the influence of a single-track momentum on the two-track correlation function. The finite momentum resolution of the detector widens the correlation function and, hence, increases the radii of the particle emission source. That effect is estimated by smearing particle momenta using the typical momentum resolution for TPCs (7%). The correction on the effect requires two versions of the femtoscopic correlation function to be built. The first function is constructed from pure generator-level events, where the momentum resolution effect is absent. The second one is calculated for the events, where momentum smearing for each particle before constructing the correlation function is performed. In this case, we will refer to estimated femtoscopic radii as $R_{i,rec}$, where i has the same meaning as in the generator-level case. The ratio of two correlation functions allows one to extract momentum resolution correction coefficients.

We will refer to the extracted femtoscopic radii estimated for the generator-level events and to the case when the momentum smearing has been performed as $R_{i,sim}$ and $R_{i,rec}$, respectively. The subscript i corresponds to the *out*, *side*, or *long* components of the femtoscopic radius, respectively. To demonstrate the effect on the extracted radii R_{out}, R_{side}, and R_{long}, the relative uncertainties $((R_{i,sim} - R_{i,rec})/R_{i,sim})$ are shown as a function of pair transverse momenta, k_T (Figure 3). The momentum resolution influence was estimated for identical pion pairs, where the influence is expected to be the largest due to the high relative yields.

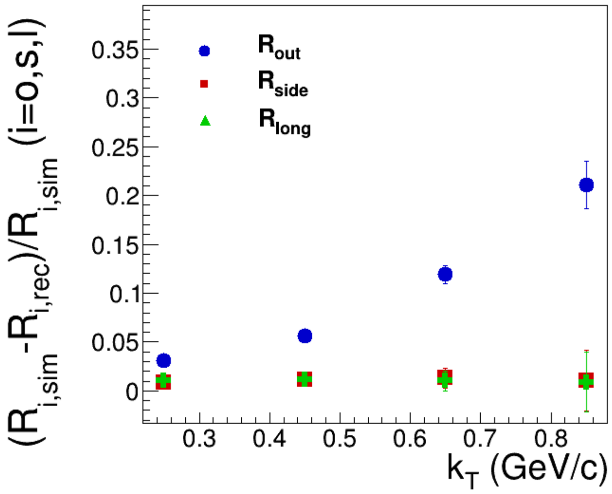

Figure 3. Relative femtoscopic radii (R_{out}, R_{side}, and R_{long}) error of the emission source radii of $\pi^+\pi^+$ pairs in Au+Au collisions. The error grows considerably in the R_{out} component, while remaining constant in other components with the increase of the mean momentum k_T. The subscripts *sim* and *rec* correspond to radii obtained from the fits to the correlation functions constructed from particles with momenta taken from the generator level and smeared according to the typical momentum resolution, respectively.

It is seen that the effect of momentum resolution affects all components of the femtoscopic radii, while being the most prominent for the outward direction (>15% effect at large k_T). This can be understood because the outward component is pointing along the transverse momentum of the pair. This clearly demonstrates the importance of the momentum resolution correction, especially at $k_T > 0.6$ GeV/c.

2.4. Factorial Moments (Intermittency) Method

Factorial moments or the intermittency method use normalized factorial moments with different normalization and averaging order. If averaging is executed firstly over bins and then over events, it is called horizontal. If ordering is changed and averaging is firstly performed over events and then over bins, it is called vertical. The definition of the normalized factorial moments with horizontal averaging (as proposed in [18]) is:

$$F_i(M) = M^{i-1} \times \langle \frac{\sum_{j=1}^{M} k_j \times (k_j - 1) \times \ldots \times (k_j - i + 1)}{N \times (N-1) \times \ldots \times (N - i + 1)} \rangle_{Events}, \tag{4}$$

where M is the number of bins in the interval, Δy, k_j is the number of particles in bin j, N is the number of particles at the interval Δy, and i is the order of the moment. Another possibility is to re-write Equation (4) using the bin size, $\delta y = \Delta y / M$:

$$F_i(M) = (\frac{\Delta y}{\delta y})^{i-1} \times \langle \frac{\sum_{j=1}^{M} k_j \times (k_j - 1) \times \ldots \times (k_j - i + 1)}{N \times (N-1) \times \ldots \times (N - i + 1)} \rangle_{Events}, \tag{5}$$

The important peculiarity of F_i^M is that no variations of this dependence are observed in the case of independent particle production, i.e., in the absence of the dynamical underlying process. In the presence of the process that introduces the positive correlation of the particles' parameters (momentum, space), F_i increases with decreasing δy. The change of F_i^M's behavior depends on the underlying processes, which define the correlation scale.

The applicability of the method to the real experiment is presented based on the simple mathematical model [61]: particles are organized into groups with centers, y_c, which are distributed uniformly along interval Δy; the number of groups is distributed according to the Poisson distribution with the mean value, λ, and the geometrical distribution with the probability α with at least one particle per group is considered to describe the number of particles in a group.

The multiplicity probability density to produce N particles in interval Δy [61] is:

$$P(N) = \sum_{m=0}^{m=N} \frac{e^{-\lambda} \lambda^m}{m!} (1 - \alpha)^{N-m} \alpha^m. \tag{6}$$

We also introduced the correlation scale fluctuating the particle position with respect to the group center by a Gaussian distribution (with σ) in the vicinity of y_c of the group. We separated two cases: the extreme case ($\sigma = 0$) is referred as the point-like group (Figure 4 (left)), while groups with $\sigma > 0$ will be labeled as non-point-like groups (Figure 4 (right).

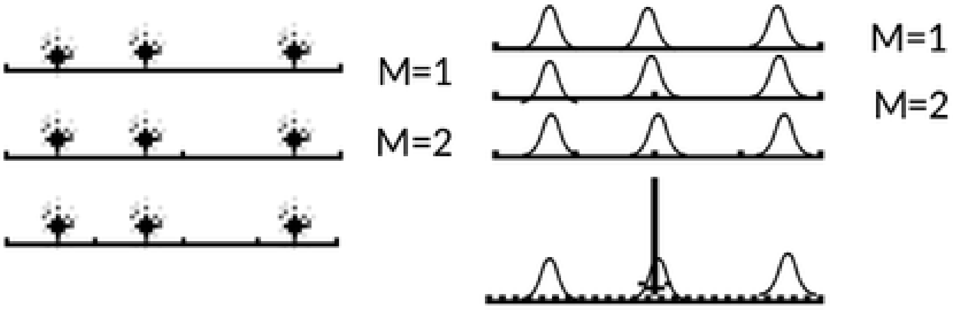

Figure 4. The consequent division of the interval Δy into bins. Particles are organized into point-like groups (**left**) and non-point-like groups (**right**).

The illustration of the $F_2(M)$ behavior in the case of independent particle production and the production of particles organized in a point-like group is presented in Figure 5 (left). The parameters of the Poisson and geometrical probability density functions are chosen to provide the mean multiplicity of particles in the interval Δy comparable with the estimations made for central events at $\sqrt{s_{NN}}$ = 7.7 GeV in $|\Delta y| < 1$, i.e., ≈100 particles/event.

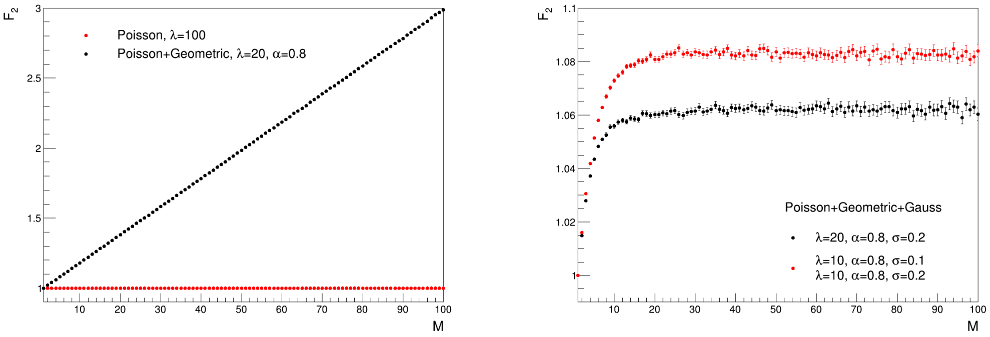

Figure 5. F_2 as a function of the number of bins, M, for point-like (**left**) and for non-point-like groups (**right**).

Within the assumption of a point-like group, $F_i(M)$ can be calculated analytically (as presented in [61]), and for such a simple mathematical model, it appears that $F_i(M)$ is the polynomial function with the order depending on the order of the factorial moment:

$$F_i(M) = \sum_{k=0}^{k=i-1} A_k M^k. \tag{7}$$

For $F_2(M)$, the parameters are: $A_0 = 1 - 2 \times (1-\alpha)(1-e^{-\lambda})/\lambda$ and $A_1 = 2 \times (1-\alpha)(1-e^{-\lambda})/\lambda$.

For non-point-like groups, the behavior of $F_i(M)$ is defined strongly by the widths of groups. For illustration, we considered two cases: only one process contributes to the particle production defining the correlation scale (σ) and two processes with different correlation scales ($\sigma_1 > \sigma_2$)—as shown in Figure 5 (right). The rise of F_2 starts to flatten when bin size $\delta y = \Delta M/M < \sigma$ when one process participates in production, while in the case of two processes, flattening starts when bin size $\delta y = \Delta M/M < \sigma_1$, and $F_2(M)$ is flat when bin size $\delta y = \Delta M/M < \sigma_2$.

If a set of processes with width hierarchy ($\sigma_1 > \sigma_2 > \cdots > \sigma_N$) contributes to particle production, flattening starts when bin size $\delta y = \Delta M/M < \sigma_1$ and flattening continues until $\delta y << \sigma_N$.

Thus, in the frame of the simple mathematical model, three parameters influence the power of growth and $F_i(M)$'s shape: the growth is inversely proportional to the mean number of groups per interval and proportional to the mean number of particles per group, and flattening depends on the width hierarchy of the characteristic processes, as described in [61,62]. This mathematical model refers to the clan model as proposed in [63]. In spite of its simplicity, the model reflects the underlying particle production dynamics [64,65].

In the case of a real detector, dynamic processes are convoluted with the apparatus function of the detector. We considered some of the detector effects, two-track spatial resolution and track reconstruction efficiency, to demonstrate how it affects the factorial moments method. Firstly, we applied detector effects to the simple mathematical model with particles generated in the point-like groups with coordinate y_c of the group uniformly distributed along the interval Δy. The normalized factorial moments as a function of the number of bins (M) is presented in Figure 6 and are referred to as as $F_2^{gen}(M)$. For each particle, we applied smearing of the coordinate using a Gaussian distribution with the width σ and 90% probability to be registered. By this procedure, we created pseudodetector data ($F_2^{rec}(M)$). The finite track resolution leads to the additional widening of the group of particles and disturbs the dependence $F_2(M)$. The behavior of the factorial moments is similar to the case of the non-point-like group (Figure 6). Detector effects can be treated using an unfolding procedure. We demonstrate the applicability of the SVD regularization using the ROOUNFOLD package [66]. The unfolding procedure is performed for the each Δy binning starting from

$M = 5$. $F_2(M)$ is calculated by Equation (4) for the fixed binning M for each event, and the histogram with an $F_2(M)$ distribution is filled (Figure 7). The mean value of this distribution over the number of events is used for the estimation of the $F_2^{rec}(M)$ dependence. For unfolding, we performed matching between the track and generator particle for each fixed binning, M, and created the response matrix $R(F_2^{genMatched}(M), F_2^{recMatched}(M))$, $purity = F_2^{recMatched}(M)/F_2^{recAll}(M)$, $acceptance = F_2^{genMatched}(M)/F_2^{genAll}(M)$, which are applied to $F_2^{rec}(M)$ as follows:

- $F_2^{rec}(M)$ is multiplied to purity and transformed into $F_2^{recMatched}(M)$ at M.
- The equation is solved by ROOUNFOLD with output $F_2^{genMatched}(M)$.
- $F_2^{genMatched}(M)$ is divided to acceptance to obtain an $F_2^{gen}(M)$ distribution.

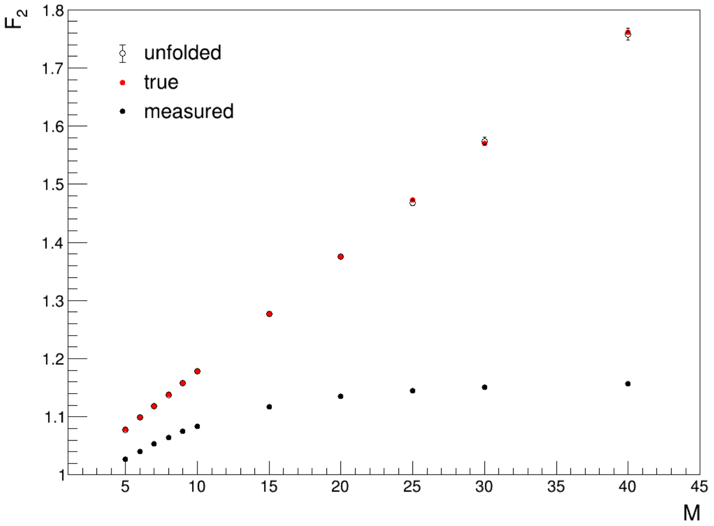

Figure 6. F_2 as a function of M for point-like group true, true with track spatial resolution applied, and unfolded.

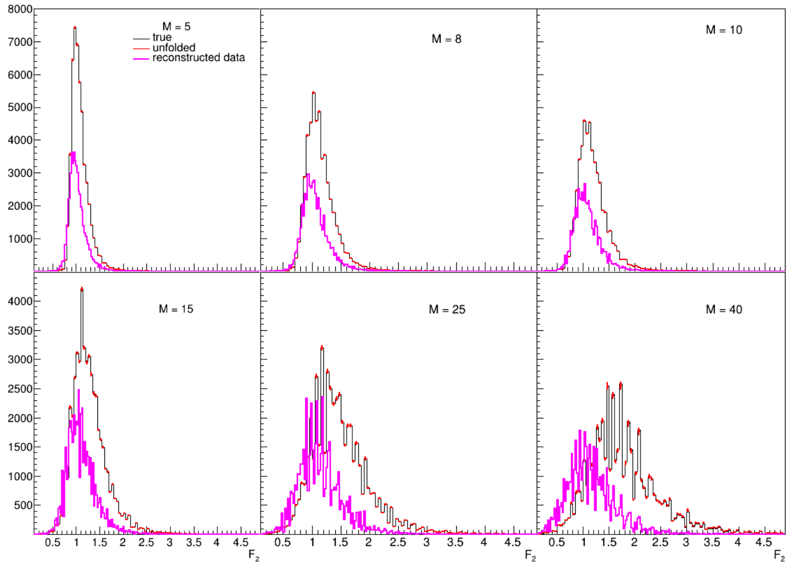

Figure 7. F_2 distribution for different divisions, true and unfolded.

The statistical errors were estimated by means of using N samples. The response matrix, purity, and efficiency were estimated with one of the samples and applied to other $N - 1$. The standard deviation of the averaged factorial moment divided by the square root of the number of samples was taken as the statistical error. Figure 6 shows the comparison of the true dependence of F_2, the true dependence after track spatial resolution is applied, and unfolded. The unfolding procedure recovers the true distribution. However, there are some factors that contribute to systematical error in this approach:

- The response matrix, purity, and acceptance are estimated over the limited number of events.
- We estimated the mean value of the factorial moment distribution (shown in Figure 7). For some distribution factorial moments, the value may appear in the overflow of the histogram, and the mean value is slightly shifted for the response matrix, purity, acceptance, and reconstructed distribution.
- We fit the plateau of the factorial moments' dependency on the number of bins using a constant function. The fit depends on the number of used divisions.
- The response matrix, purity, and acceptance are created based on some detector model and then applied to the data. Although the detector model is verified for each experiment with additional alignment and calibration measurements, the difference is unavoidable.

The shape of the factorial moment distribution for the different divisions (true, reconstructed, and unfolded) is presented in Figure 7.

The stability of the unfolding and model dependence was studied. The response matrix, acceptance, and background distributions were constructed with the fixed parameters of the Poisson and geometrical distributions, and after that, this was applied to the data generated with other parameters, as shown in Figure 8. The response matrix, purity, and acceptance were constructed with the parameters of the Poisson and geometrical distributions as shown in Figure 5, referred to as default. The parameters of the Poisson and geometrical distributions were fluctuating up to 10%, and detector smearing was applied as discussed above. After the unfolding procedure, factorial moments were compared with default values, and the difference was estimated at each number of bins M.

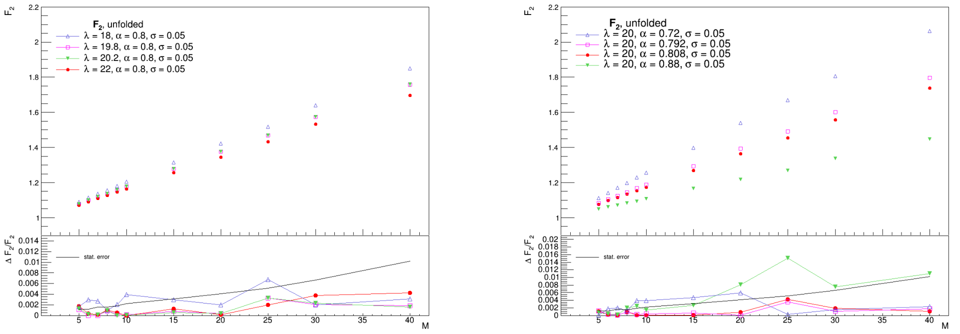

Figure 8. F_2 as a function of M unfolded for different Poisson parameters (**left**) and for different parameters of a geometrical distribution (**right**). Bottom panels show the difference between unfolded and true dependence.

3. Results

3.1. Femtoscopic Correlations of Pions and Kaons in the NICA Energy Range

In the first step of the study, the correlation functions of identical pions were constructed for the 0–5% and 10–20% central Au+Au collisions simulated at $\sqrt{s_{NN}}$ = 7.7 and 11.5 GeV in the vHLLE+UrQMD with Crossover (XPT), the First-order Phase Transition (1PT) EoS, and the UrQMD model. Figure 9 demonstrates a transverse mass (m_T) dependence of the pion femtoscopic radii R_{out} (left), R_{side} (middle), and R_{long} (right) extracted from the simulations. Red diamonds and blue and green crosses represent values obtained for UrQMD and vHLLE+UrQMD with crossover and the first-order phase transition cases.

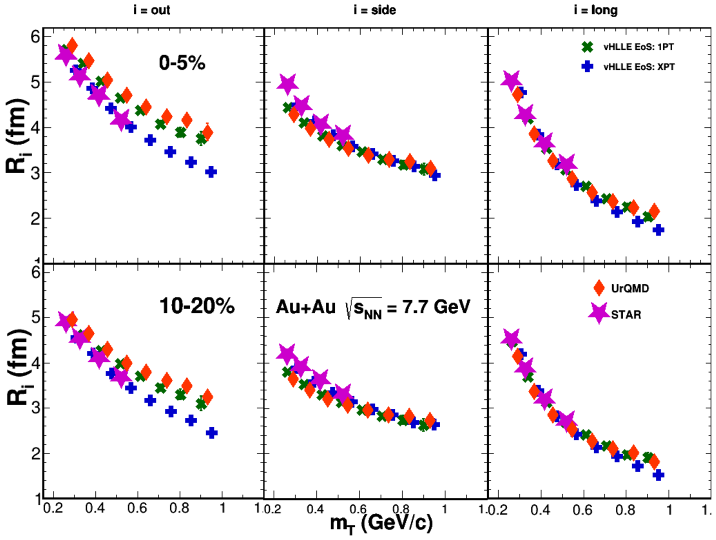

Figure 9. The transverse mass (m_T) dependence of pion femtoscopic radii R_{out} (left column), R_{side} (middle column), and R_{long} (right column) estimated for vHLLE+UrQMD with the XPT (blue crosses) and 1PT (green crosses) EoS and the UrQMD (red diamonds) models. Results are obtained for 0–5% (top row) and 10–20% central Au+Au collisions at $\sqrt{s_{NN}}$ = 7.7 GeV. Magenta stars represent pion femtoscopic radii measured by STAR [47].

The femtoscopic radii obtained from simulations in this work were compared to the experimental data (magenta stars) from the STAR experiment at RHIC [47]. It was seen that the vHLLE+UrQMD model with the crossover type of EoS showed reasonable agreement to the data.

In this paper, we extended the standard femtoscopic analysis and performed the study of the strange particles (charged kaons), thus providing the first charged kaon femtoscopic radii estimations for the NICA and RHIC energy range. Since the hybrid approach provides a reasonable description of the experimental data, the calculations of the two-kaon femtoscopic correlations was performed for two EoS scenarios in the vHLLE+UrQMD model. Figure 10 shows the estimated femtoscopic radii R_{out}, R_{side}, and R_{long} of identical pions (open symbols) and identical kaons (solid symbols) for central (0–5%) and midcentral (10–20%) Au+Au collisions at $\sqrt{s_{NN}}$ = 11.5 GeV.

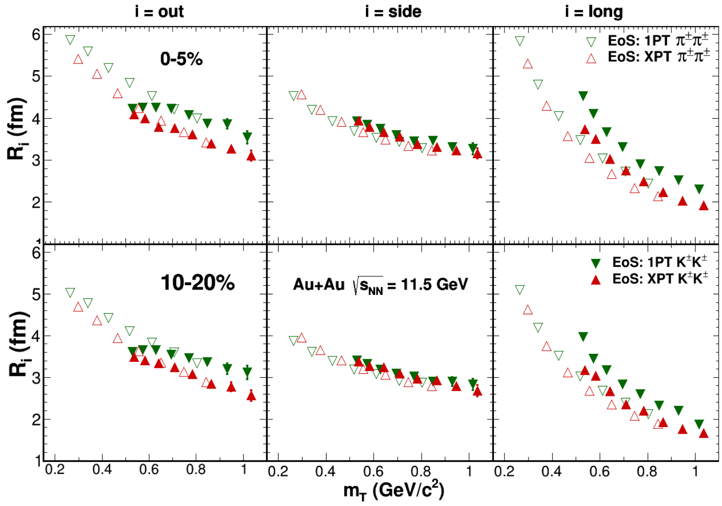

Figure 10. The m_T dependence of pion (open symbols) and kaon (solid symbols) femtoscopic radii R_{out} (left column), R_{side} (middle column), and R_{long} (right column) estimated for the vHLLE+UrQMD with the XPT (red triangles) and 1PT (green triangles) EoS for 0–5% (top row) and 10–20% central Au+Au collisions at $\sqrt{s_{NN}}$ = 11.5 GeV.

Green and red triangles shown in Figure 10 correspond to the data obtained for the simulations with the 1PT and XPT types of EoS, respectively.

3.2. Sensitivity of the Factorial Moments to the Type of Phase Transition in A+A Collisions

One of the important subject is the possibility to observe a phase transition, to determine its type, and in the best case, to find the critical point between crossover at high collision energy and first-order phase transition at low energy. We propose to use the dependence of the factorial moments on the observation window as the additional method to test the dense matter properties. Optimistic results were obtained in [23], where the possibility to distinguish the different types of phase transition (first-order phase transition, crossover, no-phase transition) in Au+Au collisions at $\sqrt{s_{NN}}$ = 7.7 and 11.5 GeV was investigated in the kinematic phase space, reachable with the MPD detector (charged particles with $p_T > 0.5$ GeV and $|y| < 1$) using Monte Carlo (MC) generators. Factorial moments $F_2(M)$ increase until the number of divisions is reached $M = 10 (\delta y = 0.2)$ and reach the plateau. The height of the plateau has a different collision energy dependence for first-order phase transition and crossover. This effect is up to 10% stable with respect to event centrality. The following studies (switching on/off cascade on top of hydrodynamic evolution) indicate that in the sequence, UrQMD+vHLLE with the following UrQMD cascade has a weak (if any) influence on the observed energy dependence of an $F_2(M)$ maximum height. The study of the $F_2(M)$ energy dependence with UrQMD (pure hadronic cascade) and HYDJET++ (absence of hadronic cascade) reveals that the effect is not present in models without explicit specification of the phase transition and is not the consequence of the collision volume shape and size. The division in this study was performed over the rapidity interval $[-1, 1]$ in [23].

The shape of the $F_2(M)$ for Au+Au collisions at 7.7 and 11.5 GeV and for two different phase transition assumptions is shown in Figure 11. The division was performed over pseudorapidity interval $[-1, 1]$. Although the height of the plateau decreases while particle rapidity (as in Ref. [23]) changes to pseudorapidity (Figure 11), the energy dependence of the plateau height is qualitatively the same.

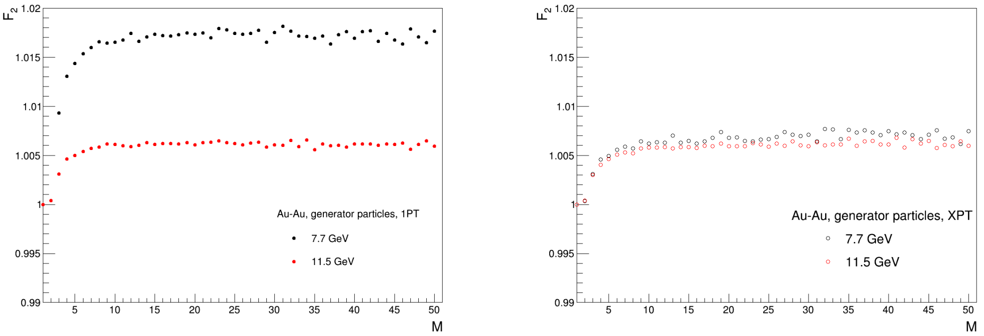

Figure 11. F_2 with generator charged particles as a function of M for Au+Au collisions with the $1^s t$-order phase transition and crossover at 7.7 GeV (**left**) and at 11.5 (**right**).

In a real detector, a set of detector effects may affect the dependence of the factorial moments on the bin size: particle identification affects the particle rapidity, finite track resolution, track reconstruction inefficiency and purity, and two-track reconstruction inefficiency. These effects can be treated in different ways. To avoid the influence of particle identification, one moves from rapidity to pseudorapidity. The effect of track resolution is shown in Section 2.4. It increases the width of the rapidity group distribution and, thus, changes the shape of the factorial moments' dependence. Track reconstruction efficiency changes the number of particles in the group, and it may change the number of groups themselves and, thus, change the strength of the multiparticle correlations or change the level of the plateau. To show the effect of track spatial resolution and track reconstruction efficiency, the pseudorapidity of each charged particle is smeared according to the detector spatial resolution.

Tracking efficiency is introduced by means of the 90% probability of the track being reconstructed. The introduction of the detector effects changes the height of the plateau, while the energy dependence is still observed. Figure 12 shows the dependence of the height of the $F_2(M)$ plateau on the collision energy for generator particles and for generator particles smeared by the detector effects.

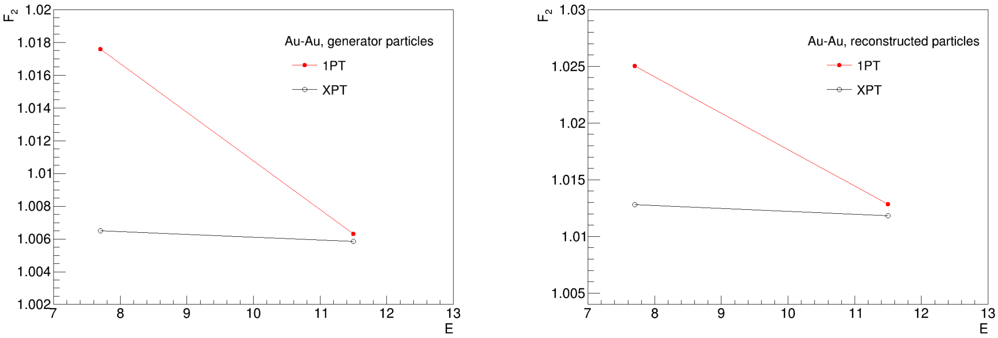

Figure 12. The maximum of $F_2(M)$ as a function of collision energy for Au+Au interactions produced with UrQMD+vHLLE (**left**), after smearing of the particles' pseudorapidity according to the detector spatial resolution and introducing 90% tracking efficiency (**right**).

The procedure of unfolding with the ROOUNFOLD package was introduced to correct the detector effects. The comparison of the reconstructed true and unfolded $F_2(M)$ as a function of M is presented in Figure 13. The difference between true and unfolded $F_2(M)$ is presented in the bottom panel and shows that $F_2(M)$ is restored with up to per-mile accuracy. The agreement of the true and unfolded dependence of the $F_2(M)$ plateau height as a function of the collision energy is shown in Figure 13 (right).

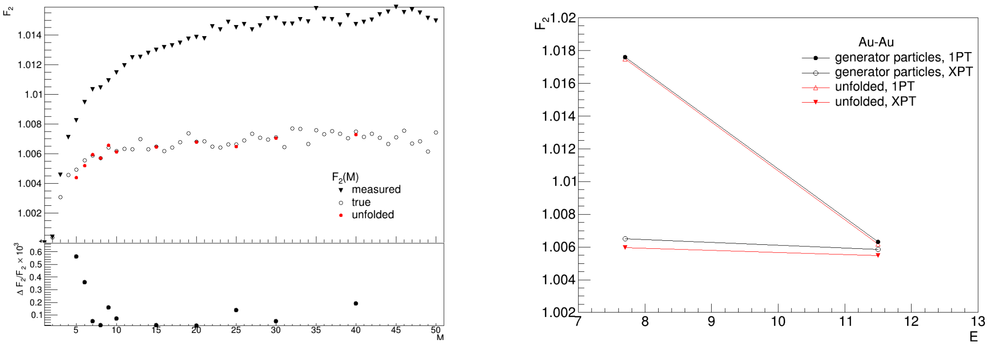

Figure 13. F_2 as a function of M reconstructed, true, and unfolded for Au+Au collisions at 11.5 GeV with crossover (**left**); the maximum of the $F_2(M)$ as a function of collision energy (**right**).

4. Discussion

4.1. Femtoscopic Correlations of Pions and Kaons

The decrease of the femtoscopic radii R_{out}, R_{side}, and R_{long} with increasing transverse mass m_T originates from the collective expansion of the particle-emitting source. The effect is qualitatively reproduced by the dynamic models UrQMD and vHLLE+UrQMD. Estimated radii decrease with collision centrality (going from central to peripheral collisions) because of the simple geometrical picture of the collision. The pion radii obtained for each collision centrality and m_T range slightly overestimate the experimental data. The vHLLE+UrQMD model with XPT EoS reproduces pion femtoscopic radii measured by STAR [47] quite well. The vHLLE+UrQMD model with the 1PT EoS overestimates measured femtoscopic radii in the outward direction, and the difference increases with m_T. Our calculations cover the m_T range from 0.2 to 0.95 GeV/c^2, which is almost two-times larger than that for the experimental data. The difference between R_{out} estimated from the hybrid model with the first-order and crossover EoS increases with the increasing transverse mass of the particle pair and reaches ∼1 fm at m_{T} = 0.9 GeV/c. The slope of m_{T}-dependence for kaons demonstrates the strong sensitivity to the EoS type. The pure UrQMD model (hadronic cascade) gives quite close results to vHLLE+UrQMD with the 1PT EoS indicating similar time delays in the process of particle emission. Such a pronounced difference between radii at high values of m_T obtained in simulations with various types of phase transitions looks very promising and motivates detailed experimental studies aimed at measuring the pion and kaon femtoscopic observables.

Since the pion femtoscopic results are well reproduced, we performed the first calculations of charged kaon correlations using the vHLLE+UrQMD model at the NICA and RHIC energy range. The behavior of the kaon and pion radii with m_T dependence was similar. Femtoscopic radii decrease with m_T and in the case of switching from central to peripheral collisions. The kaon radii decrease with m_T due to the radial flow (similar to pions). Both pions and kaons show higher radii values for the case of the 1PT EoS as compared to the XPT EoS. The m_T dependence of R_{out} and R_{side} obtained for pions and kaons is consistent with each other, indicating similar sizes of the sources and time delays in particle emission. The R_{long} values estimated for kaons are generally larger than those for pions. This difference may come from the resonance decays [33], such as K^* and ϕ mesons.

The R_{side} values obtained for the 1PT and XPT EoSs are similar, while the R_{out} and R_{long} values obtained for the case of 1PT are slightly (up to 20%) larger than those for XPT. This implies that, to measure these difference, one needs to have not just high event statistics measurements, but also control the systematic effects that may distort the femtoscopic measurements.

4.2. Intermittency Analysis

As is shown in Section 3.2, the behavior of the factorial moments depends neither on the initial state, nor on the final cascade and is insensitive to the size and shape of the interaction volume and to the maximum of the central events' multiplicity. The different dependence of the height of the factorial moments' plateau on the collision energy for the 1PT and XPT phase transition is connected to the evolution of the hydrodynamic phase as implemented in the vHLLE+UrQMD model. Note, however, that the results for $F_2(M)$ obtained with different kinds of phase transitions may be sensitive to the way of implementing the particle clustering effect in a particular model, which may allow justifying the model by comparing $F_2(M)$ results in the model and data. Therefore, further studies on this topic using the modern approaches for the model implementation of quark–hadron phase transition are needed.

4.3. Detector Effects

The influence of experimental effects such as finite momentum and spatial two-track resolutions on the measurement of pion and kaon femtoscopic correlations in modern experimental setups was estimated. The quality of two-track spatial resolution is an important detector characteristic from the femtoscopy studies' point of view. It has been demonstrated that the momentum resolution effect can lead to the distortion of femtoscopic radii (more than 15%) and shows the importance of the momentum resolution correction, especially for the large transverse pair momentum measurements ($k_T > 0.6$ GeV/c). The equation to estimate the two-track resolution for idealized characteristics of TPC was introduced.

The estimation of how the detector effects affect the factorial moments was performed. It appears that factorial moments are sensitive to particle identification, track momentum and spatial resolutions, and reconstruction efficiency. To avoid the particle misidentification and momentum resolution influence, the analysis was performed in terms of the pseudorapidity variable (η) instead of rapidity (y). The procedure to correct the detector spatial resolution and track reconstruction efficiency for factorial moments' dependency measurement with the unfolding procedure was presented. Systematic uncertainty due to the underlying model was estimated using a simple mathematical model. It appears that the change of the number of clusters (groups) and the number of particles per group up to 10% introduces less then a 2% shift of the factorial moments' values.

Thus, the importance of properly accounting for the detector effects on the femtoscopic and factorial moments' measurements was demonstrated.

5. Conclusions

We reported the results of the normalized factorial moments and femtoscopic correlations analysis in Au+Au collisions at $\sqrt{s_{NN}} = 7.7$ and 11.5 GeV using the UrQMD, vHLLE+UrQMD (with the crossover and first-order equation of states), and HYDJET++ models.

The three-dimensional femtoscopic analysis was performed for identical pion and kaon pairs. The extracted femtoscopic radii (R_{out}, R_{side}, and R_{long}) of pions and kaons decrease with increasing transverse mass m_T, showing the sensitivity to radial flow. The radii for central collisions are larger than those for midcentral ones, which reflects a simple geometrical picture of the collision. The R_{out} and R_{side} values of pions and kaons are similar for the vHLLE+UrQMD model with first-order and crossover EoSs. It was found that the femtoscopic radii of pions and kaons obtained from vHLLE+UrQMD with the first-order EoS and UrQMD (hadronic cascade) are close to each other and larger than those extracted from vHLLE+UrQMD with the crossover EoS. These observations demonstrate the relevance of using a wide m_{T} range for the femtoscopic studies and, consequently, the importance of fine two-track detector resolution. The R_{long} obtained for kaons is slightly larger than that for pions, which may be due to the contribution from the long-lived resonance decays, e.g., K^*.

The simple mathematical model shows that the number and hierarchy of the characteristic widths of the clusters, together with the number of particles within the cluster are responsible for the factorial moments' function behavior. As was shown with the vHLLE+UrQMD model, normalized factorial moments as a function of the observation interval size appeared to be sensitive to the realization of the phase transition in heavy ion collisions. In particular, it may be sensitive to the time and space evolution of the hydrodynamical phase. Neither the initial cascade, nor the final hadronic cascade introduce the strong influence of the height of the factorial moments' maxima as implemented in UrQMD. The factorial moments appeared to be a powerful tool for multiparticle correlation studies, in particular in the course of heavy ion collisions.

The importance of experimental effects, such as particle identification, single-track momentum, and two-track spatial resolutions, and methods for how to account for them, for the factorial moments and correlation femtoscopy measurements, were demonstrated. It was shown that the developed methods would provide one the principal possibility to perform the corresponding measurements in modern experimental setups.

Author Contributions: Supervision, O.K., L.M., G.N., K.M. and I.L.; Methodology, O.K., L.M., G.N., K.M., I.L. and V.K.; Project administration, L.M.; funding acquizition, L.M. and G.N.; Software, M.C., A.C., O.K., V.K., Y.K., I.L., L.M., K.M. and G.N.; formal analysis, M.C., A.C., O.K., V.K., Y.K., I.L., L.M., K.M. and G.N.; writting, G.N., L.M., I.L., O.K., V.K. and K.M.; review and editting, G.N., L.M., I.L., O.K., V.K. and K.M. All authors have read and agreed to the published version of the manuscript.

Funding: The reported study was funded by RFBR according to the Research Project No. 18-02-40044, by the Ministry of Science and Higher Education of the Russian Federation, Project "Fundamental properties of elementary particles and cosmology" No. 0723-2020-0041, and by the MEPhI Program Priority 2030.

Institutional Review Board Statement: Not applicable.

Informed Consent Statement: Not applicable.

Data Availability Statement: Not applicable.

Acknowledgments: The authors would like to thank Yu. Sinyukov, Iu. Karpenko, R. Lednický, and P. Batyuk for their great contribution to the work and the possibilities to have fruitful discussions. The work was performed using resources of the heterogeneous computing platform HybriLIT of

JINR (LIT) (http://hlit.jinr.ru) (accessed on 15 June 2022) and NRNU MEPhI high-performance computing center.

Conflicts of Interest: The authors declare no conflict of interest.

References

1. Arsene, I.; Bearden, I.G.; Beavis, D.; Besliu, C.; Budick, B.; Bøggild, C.H.G.; Chasmana, C.H.; Christensen, G.; Christiansen, P.; Cibor, J.; et al. Quark-gluon plasma and color glass condensate at RHIC? The perspective from the BRAHMS experiment. *Nucl. Phys. A* **2005**, *757*, 1–27. [CrossRef]
2. Back, B.; Baker, M.D.; Ballintijn, M.; Barton, D.S.; Becker, B.; Betts, R.R.; Bickley, A.A.; Bindel, R.; Budzanowski, A.; Busza, W.; et al. The PHOBOS perspective on discoveries at RHIC. *Nucl. Phys. A* **2005**, *757*, 28–101. [CrossRef]
3. Adams, J.; Aggarwal, M.M.; Ahammed, Z.; Amonett, J.; Anderson, B.D.; Arkhipkin, D.; Averichev, G.S.; Badyal, S.K.; Bai, Y.; Balewski, J.; et al. Experimental and theoretical challenges in the search for the quark–gluon plasma: The STAR Collaboration's critical assessment of the evidence from RHIC collisions. *Nucl. Phys. A* **2005**, *757*, 102–183. [CrossRef]
4. Adcox, K.; Adler, S.S.; Afanasiev, S.; Aidala, C.; Ajitanand, N.N.; Akiba, Y.; Al-Jamel, A.; Alexander, J.; Amirikas, R.; Aoki, K.; et al. Formation of dense partonic matter in relativistic nucleus-nucleus collisions at RHIC: Experimental evaluation by the PHENIX Collaboration. *Nucl. Phys. A* **2005**, *757*, 184–283. [CrossRef]
5. Aamodt, K.; Abelev, B.; Abrahantes Quintana, A.; Adamova, D.; Adare, A.M.; Aggarwal, M.M.; Aglieri Rinella, G.; Agocs, A.G.; Aguilar Salazar, S.; Ahammed, Z.; et al. Elliptic flow of charged particles in Pb-Pb collisions at $\sqrt{s_{NN}} = 2.76$ TeV. *Phys. Rev. Lett.* **2010**, *105*, 252302. [CrossRef]
6. Aad, G.; Abbott, B.; Abdallah, J.; Abdelalim, A.A.; Abdesselam, A.; Abdinov, O.; Abi, B.; Abolins, M.; Abramowicz, H.; Acerbi, E.; et al. Measurement of the pseudorapidity and transverse momentum dependence of the elliptic flow of charged particles in lead-lead collisions at $\sqrt{s_{NN}}$ = 2.76 TeV with the ATLAS detector. *Phys. Lett. B* **2012**, *707*, 330–348. [CrossRef]
7. Chatrchyan, S.; Khachatryan, V.; Sirunyan, A.M.; Tumasyan, A.; Adam, W.; Bergauer T.; Dragicevic, M.; Ero, J.; Fabjan, C.; Friedl, M.;et al. Measurement of the elliptic anisotropy of charged particles produced in PbPb collisions at $\sqrt{s_{NN}} = 2.76$ TeV. *Phys. Rev. C* **2013**, *87*, 014902. [CrossRef]
8. Gyulassy, M.; McLerran, L. New forms of QCD matter discovered at RHIC. *Nucl. Phys. A* **2005**, *750*, 30–63. [CrossRef]
9. Aoki, Y.; Endrodi, G.; Fodor, Z.; Katz, S.D.; Szabo, K.K. The order of the quantum chromodynamics transition predicted by the standard model of particle physics. *Nature* **2006**, *443*, 675–678. [CrossRef]
10. Ejiri, S. Canonical partition function and finite density phase transition in lattice QCD. *Phys. Rev. D* **2008**, *78*, 074507. [CrossRef]
11. Stephanov, M. QCD phase diagram and the critical point. *Prog. Theor. Phys. Suppl.* **2004**, *153*, 139–156. [CrossRef]
12. Hatta, Y.; Stephanov, M. Proton-number fluctuation as a signal of the QCD critical end point. *Phys. Rev. Lett.* **2003**, *91*, 129901. [CrossRef]
13. Borsanyi, S.; Fodor, Z.; Guenther, J.N.; Katz, S.K.; Pasztor, A.; Portillo, I.; Ratti, C.; Szabó, K.K. Towards the equation of state at finite density from the lattice. *Nucl. Phys. A* **2019**, *982*, 223–226. [CrossRef]
14. Bazavov, A.; Bollweg, D.; Ding,H.-T.; Enns, P.; Goswami, J.; Hegde, P.; Kaczmarek, O.; Karsch, F.; Larsen, R.; Mukherjee, S.; et al. Skewness, kurtosis, and the fifth and sixth order cumulants of net baryon-number distributions from lattice QCD confront high-statistics STAR data. *Phys. Rev. D* **2020**, *101*, 074502. [CrossRef]
15. Abdallah, M.S.; Adam, J.; Adamczyk, L.; Adams, J.R.; Adkins, J.K.; Agakishiev, G.; Aggarwal, I.; Aggarwal, M.; Ahammed, Z.; Alekseev, I.; et al. Measurement of the sixth-order cumulant of net-proton multiplicity distributions in Au + Au collisions at $\sqrt{s_{NN}} = 27, 54.4,$ and 200 GeV at RHIC. *Phys. Rev. Lett.* **2021**, *127*, 262301. [CrossRef]
16. Fraga, E.; Kodama, T.;Palhares, L.F.; Sorensen, P. Finite-size effects and the search for the critical endpoint of QCD. *PoS FACES QCD* **2010**, *117*, 17.
17. Adam, J.; Adamczyk, L.; Adams, J.R.; Adkins, J.K.; Agakishiev, G.; Aggarwal, M.M.; Ahammed, Z.; Alekseev, I.; Anderson, D.M.; Aparin, A.; et al. Nonmonotonic energy dependence of net-proton number fluctuations. *Phys. Rev. Lett.* **2021**, *126*, 092301. [CrossRef]
18. Bialas, A.; Peschanski, R. Moments of rapidity distributions as a measure of short-range fluctuations in high-energy collisions. *Nucl. Phys.* **1986**, *B273*, 703. [CrossRef]
19. Antoniou, N.G.; Davis, N.N.; Diakonos, F.K. Improved intermittency analysis of proton density fluctuations in NA49 ion collisions at 158 AGeV. *EPJ Web Conf.* **2014**, *71*, 00035. [CrossRef]
20. Khan, M.M.; Hussain, T.; Das, I.; Ahmad, S.; Chattopadhyay, S. Improved intermittency analysis of charged particle density fluctuations in Pb+Pb collisions at $\sqrt{s_{NN}}$ = 2.76 TeV. *DAE-BRNS. Symp. Nucl. Phys.* **2016**, *61*, 840.
21. Davis, N. Searching for the Critical Point of Strongly Interacting Matter in Nucleus–Nucleus Collisions at CERN SPS. *Acta Phys. Polon. Supp.* **2020**, *13*, 637–643. [CrossRef]
22. Anticic, T.; Baatar, B.; Barna, D.; Bartke, J.; Beck, J.; Betev, L.; Białkowska, H.; Blume, C.; Bogusz, M.; Boimska B.; et al. Critical fluctuations of the proton density in A+A collisions at 158A GeV. *Eur. Phys. J. C* **2015**, *75*, 587. [CrossRef]
23. Kodolova, O.; Cheremnova, M.; Lokhtin, I.; Chernyshov, A.; Malinina, L.; Mikhaylov, K.; Batyuk, P.; Nigmatkulov, G. Factorial Moments in the NICA/MPD Experiment. *Phys. Part. Nucl.* **2021**, *52*, 658–662. [CrossRef]

24. Lisa, M.; Frodermann, E.; Graef, G.; Mitrovski, M.; Mount, E.; Petersen, H.; Bleicher, M. Shape analysis of strongly interacting systems: The heavy ion case. *New J. Phys.* **2011**, *13*, 065006. [CrossRef]
25. Kopylov, G.I.; Podgoretsky, M. Correlations of identical particles emitted by highly excited nuclei. *Sov. J. Nucl. Phys.* **1972**, *15*, 219.
26. Kopylov, G. Like particle correlations as a tool to study the multiple production mechan. *Phys. Lett. B* **1974**, *50*, 472–474. [CrossRef]
27. Podgoretsky, M.I. Identical pion interferometry correlations. Theory. *Sov. J. Part. Nucl.* **1989**, *20*, 266.
28. Lisa, M.A.; Pratt, S.; Soltz, R.; Wiedemann, U. Femtoscopy in relativistic heavy ion collisions: Two decades of progress. *Ann. Rev. Nucl. Part. Sci.* **2005**, *55*, 357–402. [CrossRef]
29. Akkelin, S.V.; Sinyukov, Y.M. The HBT-interferometry of expanding sources. *Phys. Lett. B* **1995**, *356*, 525–530. [CrossRef]
30. Kravchenko, Y.V.; Khyzhniak, Y.V.; Bravina, L.V.; Nigmatkulov, G.A.; Sinyukov, Y.M.; Zabrodin, E.E. Space-time structure of the pion emission in central Au+Au collisions at RHIC energies. *Phys. Scr.* **2021**, *96*. [CrossRef]
31. Adams, J.; Aggarwal, M.M.; Ahammed, Z.; Amonett, J.; Anderson, B.D.; Arkhipkin, D.; Averichev, G.S.; Badyal, S.K.; Bai, Y.; Balewski, J.; et al. Pion interferometry in Au+Au collisions at $\sqrt{s_{NN}} = 200$ GeV. *Phys. Rev. C* **2005**, *71*, 044906. [CrossRef]
32. Adam, J.; Adamova, D.; Aggarwal, M.M.; Aglieri Rinella, G.; Agnello, M.; Agrawal, N.; Ahammed, Z.; Ahn, S.U.; Aimo, I.; Aiola S.; et al. Centrality dependence of pion freeze-out radii in Pb-Pb collisions at $\sqrt{s_{NN}} = 2.76$ TeV. *Phys. Rev. C* **2016**, *93*, 024905. [CrossRef]
33. Shapoval, V.M.; Sinyukov, Y.M. Kaon and pion maximal emission times extraction from the femtoscopy analysis of 5.02A TeV LHC collisions within the integrated hydrokinetic model. *Nucl. Phys. A* **2021**, *1016*, 122322. [CrossRef]
34. Acharya, S.; Adam, J.; Adamova, D.; Adolfsson, J.; Aggarwal, M.M.; Aglieri Rinella, G.; Agnello, M.; Agrawal, N.; Ahammed, Z.; Ahmad, N.; et al. Kaon femtoscopy in Pb-Pb collisions at $\sqrt{s_{NN}} = 2.76$ TeV. *Phys. Rev. C* **2017**, *96*, 064613. [CrossRef]
35. Shapoval, V.M.; Braun-Munzinger, P.; Karpenko, Y.M.; Sinyukov, Y.M. Femtoscopy correlations of kaons in Pb+Pb collisions at LHC within hydrokinetic model. *Nucl. Phys. A* **2014**, *929*, 1–8. [CrossRef]
36. Pratt, S. Pion interferometry of quark–gluon plasma. *Phys. Rev. D* **1986**, *33*, 1314–1327. [CrossRef]
37. Bertsch, G.; Gong, M.; Tohyama, M. Pion interferometry in ultrarelativistic heavy-ion collisions. *Phys. Rev. C* **1988**, *37*, 1896–1900. [CrossRef]
38. Rischke, D.H.; Gyulassy, M. The time-delay signature of quark–gluon plasma formation in relativistic nuclear collisions. *Nucl. Phys. A* **1996**, *608*, 479–512. [CrossRef]
39. Adler, C.; Aggarwal, M.M.; Ahammed, Z.; Amonett, J.; Anderson, B.D.; Arkhipkin, D.; Averichev, G.S.; Badyal, S.K.; Bai, Y.; Balewski, J.; et al. Pion interferometry of $\sqrt{s_{NN}} = 130$ GeV $Au + Au$ collisions at RHIC. *Phys. Rev. Lett.* **2001**, *87*, 082301. [CrossRef]
40. Adcox, K.; Adler, S.S.; Ajitanand, N.N.; Akiba, Y.; Alexander, J.; Aphecetche, L.; Arai, Y.; Aronson, S.H.; Averbeck, R.; Awes, T.C.; et al. Centrality dependence of $\pi^{+/-}$, $K^{+/-}$, p, and $\overline{p}$ production from $\sqrt{s_{NN}} = 130$ GeV Au+Au collisions at RHIC. *Phys. Rev. Lett.* **2002**, *88*, 242301. [CrossRef]
41. Heinz, U.; Kolb, P. Early thermalization at RHIC. *Nucl. Phys. A* **2002**, *702*, 269–280. [CrossRef]
42. Shapoval, V.; Adzhymambetov, M.D.; Sinyukov, Y.M. Femtoscopy scales and particle production in the relativistic heavy ion collisions from Au+Au at 200 AGeV to Xe+Xe at 5.44 ATeV within the integrated hydrokinetic model. *Eur. Phys. J. A* **2020**, *56*, 260. [CrossRef]
43. Sinyukov, Y.M.; Akkelin, S.V.; Karpenko, I.A.; Hama, Y. Kinetics versus hydrodynamics: Generalization of Landau/Cooper-Frye prescription for freeze-out. *Acta Phys. Polon. B* **2009**, *40*, 1025–1036.
44. Broniowski, W.; Chojnacki, M.; Florkowski, W.; Kisiel, A. Uniform description of soft observables in heavy-ion collisions at $\sqrt{s_{NN}} = 200$ GeV. *Phys. Rev. Lett.* **2008**, *101*, 022301. [CrossRef] [PubMed]
45. Pratt, S. The long slow death of the HBT puzzle. *Nucl. Phys. A* **2009**, *830*, 51C–57C. [CrossRef]
46. Karpenko, I.; Bleicher, M.; Huovinen, P.; Petersen, H. Effects of EoS in viscous hydro + cascade model for the RHIC Beam Energy Scan. *Nucl. Phys. A* **2016**, *956*, 834–837. [CrossRef]
47. Adamczyk, L.; Adkins, J.K.; Agakishiev, G.; Aggarwal, M.M.; Ahammed, Z.; Alekseev, I.; Alford, J.;Anson, C.D.; Aparin, A.; Arkhipkin, D.; et al. Beam-energy-dependent two-pion interferometry and the freeze-out eccentricity of pions measured in heavy ion collisions at the STAR detector. *Phys. Rev. C* **2015**, *92*, 014904. [CrossRef]
48. Batyuk, P.; Karpenko, Y.; Lednicky, R.; Malinina, L.; Mikhaylov, K.; Rogachevsky, O.; Wielanek, D. Correlation femtoscopy study at energies available at the JINR Nuclotron-based Ion Collider fAcility and the BNL Relativistic Heavy Ion Collider within a viscous hydrodynamic plus cascade model. *Phys. Rev. C* **2017**, *96*, 024911. [CrossRef]
49. Bass, S.A.; Belkacem, M.; Bleicher, M.; Brandstetter, M.; Bravina, L.; Ernst, C.; Gerland, L.; Hofmann, M.; Hofmann, S.; Konopka, J.; et al. Microscopic models for ultrarelativistic heavy ion collisions. *Prog. Part. Nucl. Phys.* **1998**, *41*, 225. [CrossRef]
50. Bleicher, M.; Zabrodin, E.; Spieles, C.; Bass, S.A.; Ernst, C.; Soff, S.; Bravina, L.; Belkacem, M.; Weber, H.; Stöcker, H.; Greiner, W. Relativistic hadron-hadron collisions in the ultra-relativistic quantum molecular dynamics model. *J. Phys. G Nucl. Part. Phys.* **1999**, *25*, 1859. [CrossRef]
51. Karpenko, I.A.; Huovinen, P.; Petersen, H.; Bleicher, M. Estimation of the shear viscosity at finite net-baryon density from A+A collision data at $\sqrt{s_{NN}} = 7.7$–200 GeV. *Phys. Rev. C* **2015**, *91*. [CrossRef]
52. Lokhtin, I.P.; Malinina, L.V.; Petrushanko, S.V.; Snigirev, A.M.; Arsene, I.; Tywoniuk, K. Heavy ion event generator HYDJET++ (HYDrodynamics plus JETs). *Comput. Phys. Commun.* **2009**, *180*, 779–799. [CrossRef]

53. Steinheimer, J.; Schramm, S.; Stöcker, H. An effective chiral hadron-quark equation of state. *J. Phys. G Nucl. Part. Phys.* **2011**, *38*, 035001. [CrossRef]
54. Kolb, P.F.; Sollfrank, J.; Heinz, U. Anisotropic transverse flow and the quark–hadron phase transition. *Phys. Rev. C* **2000**, *62*, 054909. [CrossRef]
55. Koonin, S. Proton pictures of high-energy nuclear collisions. *Phys. Lett. B* **1977**, *70*, 43–47. [CrossRef]
56. Ackermann, K.H.; Adams, N.; Adler, C.; Ahammed, Z.; Ahmad, S.; Allgower, C.; Amonett, J.; Amsbaugh, J.; Anderson, B.D.; Anderson, M.; et al. STAR Detector Overview. *Nucl. Instrum. Meth.* **2003**, *A 499*, 624–632. [CrossRef]
57. Aamodt, K.; Quintana, A.A.;Achenbach, R.;Acounis, S.;Adamova, D.; Adler, C.; Aggarwal, M.; Agnese, F.; Rinella, G.A.; Ahammed, Z.; Ahmad, A.; et al. The ALICE experiment at the CERN LHC. *JINST* **2008**, *3*, S08002. [CrossRef]
58. Alme, J.; Andres, Y.; Appelshauser, H.; Bablok, S.; Bialas, N.; Bolgen, R.; Bonnes, U.; Bramm, R.; Braun-Munzinger, P.; Campagnolo, R.; et al. The ALICE TPC, a large 3-dimensional tracking device with fast readout for ultra-high multiplicity events. *Nucl. Instrum. Meth. A* **2010**, *622*, 316–367. [CrossRef]
59. Anderson, M.; Berkovitz, J.; Betts, W.; Bossingham, R.; Bieser, F.; Brown, R.; Burks, M.; de la Barca Sánchez, M.C.; Cebra, D.; Cherney, M.; et al. The STAR time projection chamber: A unique tool for studying high multiplicity events at RHIC. *Nucl. Instrum. Meth. A* **2003**, *499*, 659–678. [CrossRef]
60. Abraamyan, K.U.; Afanasiev, S.V.; Alfeev, V.S.; Anfimov, N.; Arkhipkin, D.; Aslanyan, P.Z.; Babkin, V.A.; Baznat, M.I.; Bazylev, S.N.; Blaschke, D.; et al. The MPD detector at the NICA heavy-ion collider at JINR. *Nucl. Instrum. Meth. A* **2011**, *628*, 99–102. [CrossRef]
61. Bogolyubsky, M.Y.; Levitskii, M.S.; Maksimov, V.V.; Minaenko, A.A.; Moiseev, A.M.; Chekulaev, S.V.; Bravina, L.V.; Zabrodin, E.E. Kodolova, O.L.; Kruglov, N.A.; et al. Clan model and factorial moments of the multiplicity distribution in intervals. *Phys. Atom. Nucl.* **1994**, *57*, 2132.
62. Bogolyubsky, M.Y.; Levitskii, M.S.; Maksimov, V.V.; Minaenko, A.A.; Moiseev, A.M.; Chekulaev, S.V.; Bravina, L.V.; Zabrodin, E.E.; Kodolova, O.L.; Kruglov, N.A.; et al. Characteristics of the groups of charged particles in pbar p, pp and K-p interactions at 32 GeV/c. *Phys. Atom. Nucl.* **1995**, *58*, 1984.
63. Giovannini, A.; Van Hove, L. Negative Binomial Properties and Clan Structure in Multiplicity Distributions. *Acta Phys. Polon. B* **1988**, *19*, 495.
64. Bhaduri, S.; Bhaduri, A.; Ghosh, D. Clan-Model of Particle Production Process-Revisited in Chaos-based Complex Network Scenario. *Phys. Part. Nucl. Lett.* **2018**, *15*, 446–455. [CrossRef]
65. Giovannini, A.; Ugoccioni, R. Clan structure analysis and QCD parton showers in multiparticle dynamics: An Intriguing dialog between theory and experiment. *Int. J. Mod. Phys. A* **2005**, *20*, 3897–4000. [CrossRef]
66. Adye, T. Unfolding algorithms and tests using RooUnfold. In Proceedings of the PHYSTAT 2011 Workshop on Statistical Issues Related to Discovery Claims in Search Experiments and Unfolding, Geneva, Switzerland, 17–20 January 2011; pp. 313–318. [CrossRef]